

SUPERMASSIVE BLACK HOLES WITH HIGH ACCRETION RATES IN ACTIVE GALACTIC NUCLEI. III. DETECTION OF Fe II REVERBERATION IN NINE NARROW-LINE SEYFERT 1 GALAXIES

CHEN HU¹, PU DU¹, KAI-XING LU^{2,1}, YAN-RONG LI¹, FANG WANG⁶, JIE QIU¹, JIN-MING BAI⁶,
SHAI KASPI⁷, LUIS C. HO^{4,5}, HAGAI NETZER⁷, JIAN-MIN WANG^{1,3,*}
(SEAMBH COLLABORATION)

Accepted for publication in The Astrophysical Journal

ABSTRACT

This is the third in a series of papers reporting on a large reverberation-mapping campaign aimed to study the properties of active galactic nuclei (AGNs) with high accretion rates. We present new results on the variability of the optical Fe II emission lines in 10 AGNs observed by the Yunnan Observatory 2.4m telescope during 2012–2013. We detect statistically significant time lags, relative to the AGN continuum, in nine of the sources. This accurate measurement is achieved by using a sophisticated spectral fitting scheme that allows for apparent flux variations of the host galaxy, and several narrow lines, due to the changing observing conditions. Six of the newly detected lags are indistinguishable from the H β lags measured in the same sources. Two are significantly longer and one is slightly shorter. Combining with Fe II lags reported in previous studies, we find a Fe II radius–luminosity relationship similar to the one for H β , although our sample by itself shows no clear correlation. The results support the idea that Fe II emission lines originate in photoionized gas which, for the majority of the newly reported objects, is indistinguishable from the H β -emitting gas. We also present a tentative correlation between the lag and intensity of Fe II and H β and comment on its possible origin.

Subject headings: galaxies: active — galaxies: nuclei — galaxies: Seyfert — methods: data analysis — quasars: emission lines

1. INTRODUCTION

Most active galactic nuclei (AGNs) show prominent Fe II emission lines in their spectra. The lines appear in several broad bands that represent thousands of individual transitions. The stronger bands cover the ranges of 4000–5400 Å (hereafter optical Fe II lines), 2800–3500 Å and 2000–2600 Å (hereafter UV Fe II lines; e.g., Wills et al. 1985; Sulentic et al. 2000; Hu et al. 2008 and references therein). The strongest Fe II lines (relative to H β) are observed in narrow-line Seyfert 1 galaxies (NLS1s, see, e.g., Osterbrock & Pogge 1985; Boller et al. 1996). Such objects are characterized by: 1) narrow ($< 2000 \text{ km s}^{-1}$) broad emission lines; 2) weak [O III] line; 3) and steep hard X-ray spectrum. These objects are found usually at the extreme end of the so-called Eigenvector 1 sequence (Boroson & Green 1992; Sulentic et al. 2000; Shen & Ho 2014) indicating high Eddington ratios and several other properties that are not fully understood.

Some NLS1s show evidence for super-Eddington accretion, with $L_{\text{bol}}/L_{\text{Edd}} > 1$. We refer to these objects as super-Eddington accreting massive black holes (SEAMBHs). Our earlier work (Wang et al. 2013, 2014) show that such objects

are potentially a new kind of standard candle for cosmology. To test this idea, and to study in more detail the physical properties of extreme NLS1s, we have initiated a large reverberation mapping (RM) campaign to measure, accurately, the black hole (BH) mass of such sources. The initial results of this campaign have been published in Du et al. (2014, hereafter Paper I) and Wang et al. (2014, Paper II). The present paper, the third in this series, is dedicated to the study of Fe II emission lines in our sample of SEAMBH candidates. A fourth paper, submitted in parallel to this one, presents new data on H β time lags and BH mass in five extreme SEAMBHs and focuses on the modification of the $R_{\text{BLR}}-L$ relationship in AGNs (e.g., Kaspi et al. 2000, 2005; Bentz et al. 2013) in the presence of such sources.

The excitation mechanism of the Fe II emission in AGNs has been discussed in numerous publications (e.g., Collin-Souffrin et al. 1980; Netzer & Wills 1983; Joly 1987; Sigut & Pradhan 1998; Baldwin et al. 2004; Ferland et al. 2009). Most of these studies suggest an origin in the broad-line region (BLR) but the line intensities calculated so far are in poor agreement with most observations. Other suggestions connect these lines to the outer part of the central accretion disk (e.g., Joly 1987) but the agreement with observations is still poor. In particular, none of the existing models can explain, satisfactorily, the relative intensity of the UV and optical Fe II lines and the observed Fe II spectrum in the range 2000–2600 Å. Line variability is an important tool in such studies since it can indicate, given a measured time lag relative to the continuum variations, the location of the Fe II-emitting gas. Such variations have been detected in a number of sources (e.g., Boksenberg & Netzer 1977; Maoz et al. 1993; Kollatschny et al. 2000; Vestergaard & Peterson 2005; Wang et al. 2005; Kuehn et al. 2008; Shapovalova et al. 2012), but robust lag measurements were not obtained. This situation has changed, recently. Bian et al. (2010) revisited the data of PG 1700+518 from Kaspi et al. (2000) and mea-

¹ Key Laboratory for Particle Astrophysics, Institute of High Energy Physics, Chinese Academy of Sciences, 19B Yuquan Road, Beijing 100049, China

² Department of Astronomy, Beijing Normal University, Beijing 100875, China

³ National Astronomical Observatories of China, Chinese Academy of Sciences, 20A Datun Road, Beijing 100020, China

⁴ Kavli Institute for Astronomy and Astrophysics, Peking University, Beijing 100871, China

⁵ Department of Astronomy, School of Physics, Peking University, Beijing 100871, China

⁶ Yunnan Observatories, Chinese Academy of Sciences, Kunming 650011, China

⁷ School of Physics and Astronomy and the Wise Observatory, Tel-Aviv University, Tel-Aviv 69978, Israel

* Corresponding author

sured the light curve of the optical Fe II lines. They obtained a significant time lag relative to the 5100 Å continuum albeit with a very large uncertainty. Rafter et al. (2013) and Chelouche et al. (2014) adopted the multivariate correlation function (MCF) scheme of Chelouche & Zucker (2013) designed for photometric RM. Rafter et al. (2013) studied the NLS1 SDSS J113913.91+335551.1 using RM and found the Fe II time lag is consistent with the one of the H β line. Chelouche & Zucker (2013) measured optical Fe II light curves, and time lags, for three of the objects in Kaspi et al. (2000), one of which is the object studied by Bian et al. (2010). They also find somewhat less significant Fe II time lag for three other sources. Chelouche & Zucker (2013) presents a tentative Fe II size-luminosity relation and suggest that the Fe II emission-region size is comparable to that of the H β line. Barth et al. (2013) used spectroscopic measurements of optical Fe II lines and found lags that are 1.5 and 1.9 times longer than the corresponding H β . All these studies confirm the photoionization origin of the Fe II lines. The success of the Barth et al. (2013) campaign is due both to the detailed and frequent spectroscopic observations and a novel method they used to correct for the host galaxy contribution to the optical spectra.

This paper presents the results obtained, so far, to measure the time lags of the optical Fe II lines (hereafter Fe II lines) in our SEAMBH campaign. We have attempted to detect such lags in 10 of the sources and were able to obtain statistically significant results in nine of them. In six of the newly measured sources, the Fe II lag is entirely consistent with the H β lag and in two others it is considerably longer. Section 2 gives a brief review of the observations and data reduction. Section 3 describes our spectral fitting method, with emphasis on host galaxy and narrow line subtraction which we find to be crucial to the analysis. More details are given in Appendix A. Section 4 presents Fe II light curves and their analysis for both Fe II and H β , and compares the results of the new H β lags to those presented in Paper I and Paper II. In Section 5, we plot the size-luminosity relation for Fe II and compare the lag and intensity of Fe II with H β . The implications and some additional interpretation are also discussed. Section 6 gives a summary of the new results.

2. OBSERVATIONS AND DATA REDUCTIONS

The details of the SEAMBH campaign, including the observations, data reduction and analysis, were presented in Paper I and Paper II. For completeness, we summarize the more important points below and discuss in detail the new method of galaxy and narrow line subtraction.

2.1. Sample

Ten NLS1s identified as SEAMBH candidates were observed, spectroscopically and photometrically, between October 2012 and June 2013. Objects names and coordinates are listed in Table 1 of Paper II. H β time lags for three of the sources (Mrk 335, Mrk 142, IRAS F12397+3333) are presented in Paper I and for five additional sources (Mrk 1044, Mrk 382, MCG +06–26–012, Mrk 486, Mrk 493) in Paper II. Like many other NLS1s (Boroson & Green 1992; Sulentic et al. 2000; Boroson 2002; Zhou et al. 2006, e.g.), all the sources in our sample show strong Fe II emission lines and high $L_{\text{bol}}/L_{\text{Edd}}$. This sample is, therefore, different from most AGNs in the local universe and none of the results presented below should be compared with earlier studies, like Hu et al. (2008) that address the general population properties.

2.2. Spectroscopy and Data Reduction

The spectra were obtained using the Yunnan Faint Object Spectrograph and Camera (YFOSC), mounted on the Lijiang 2.4m telescope at Yunnan Observatory of the Chinese Academy of Sciences. A longslit with projected width of 2''5 was oriented to take the spectra of the object and a nearby non-varying comparison star simultaneously following, e.g., Maoz et al. (1990) and Kaspi et al. (2000). The comparison star is then used as a standard for flux calibration. For the Lijiang 2.4m telescope, the rotator is accurate and the tracking is stable. Thus the object and the comparison star were kept within the slit during the typical 30 min. exposures. The distance between the object and the comparison star along the direction of slit width keeps less than 1 pixel (0''283).

Grism 14 was used and yielded spectra covering the wavelength range of 3800–7200 Å with a dispersion of 1.8 Å pixel⁻¹. The final spectral resolution, obtained by comparing the width of the [O III] emission line with the one measured from the Sloan Digital Sky Survey (SDSS; York et al. 2000) spectrum of the same object, is roughly 500 km s⁻¹. All spectra are extracted in a uniform, large aperture of 8''5 to minimize light losses. The flux calibration is based on the comparison of the object flux to the comparison star flux in the 2''5 × 8''5 apertures. However, the host galaxy flux calibration is different because of the non-stellar image — the galaxy is extended and resolved. This can result in apparent flux variations due to variable seeing and mis-centering. This requires a different calibration procedure that has a large impact on the various light curves. Appendix A gives details of this procedure.

3. LINE AND CONTINUUM MEASUREMENTS

3.1. Fitting scheme

The traditional method to measure the flux of the continuum and the broad emission lines, in most RM studies, is simple integration (e.g., Kaspi et al. 2000). A straight line is set between two line-free windows to define the AGN continuum, and the flux of the emission line is measured by simple integration above the line. This method works well for single, strong emission lines, e.g., H β , because there are no (or only weak) other emission lines in this range and the wavelength window is narrow enough for the continuum to be approximated by a straight line. In the case of Fe II, neither condition is satisfied.

Fe II emission consists of thousands of lines that form a pseudo-continuum. The most prominent features in the optical band are two bumps between 4500 to 5500 Å: one between H β and H γ , and the other on the red side of [O III] λ 5007. Even for quasars, whose host galaxies are extremely faint relative to the AGN, it is hard to find “pure” continuum windows, and it is inappropriate to assume a straight line over such a wide wavelength range of more than 1000 Å. The strong host galaxy contribution in most of our objects, and the contamination by other emission lines (e.g., He II and coronal lines), make the situation much worse. Appendix B presents the Fe II light curves measured by the traditional integration method. All light curves have large scatter, and only less than a half show rough structures. A simultaneous fitting including the Fe II emission and all the other spectral components is necessary.

Template-fitting is a widely used method to measure Fe II emission in single-epoch spectra of AGNs (see, e.g., Hu et al. 2008 for a brief overview). Input-output simulations show

that template-fitting is a reliable measurement of Fe II emission with equivalent width (EW) $> 25 \text{ \AA}$ in quasars (Hu et al. 2008). It is also common to include a host galaxy component into the fitting of Type I AGNs with strong host contribution (e.g., Zhou et al. 2006; Ho & Kim 2009). The method has been adopted, recently, to measure the light curves in a few reverberation mapping studies, and proved to be successful. Bian et al. (2010) reanalyzed the spectra of PG 1700+518, using data from Kaspi et al. (2000). They detected a lag of 209_{-147}^{+100} days for Fe II emission. Barth et al. (2013) performed a very careful spectral decomposition including a power-law continuum, a host galaxy component, Fe II template, and other emission lines (H β , [O III], He II, and He I). Using this technique they were able to obtain statistically significant reverberation lags of the Fe II lines in two Seyfert 1 galaxies, NGC 4593 and Mrk 1511.

The spectral fitting in the present paper follows the algorithm of Hu et al. (2012), where several spectral components are fitted simultaneously by minimizing the χ^2 via Levenberg-Marquardt method. All the light curves are obtained directly from the results of the fitting. Before fitting, we correct the calibrated spectra for Galactic extinction and redshift. We use the R_V -dependent Galactic extinction law given by Cardelli et al. (1989) and O'Donnell (1994) and R_V is assumed to be 3.1. The redshift z and V -band extinction are taken from the NASA/IPAC Extragalactic Database⁹ and Schlafly & Finkbeiner (2011), as listed in Papers I and II.

The left panel of Figure 1 shows the fitting to the spectrum of Mrk 382 taken at Julian date (JD) 2456298, after Galactic extinction and redshift correction. The fitting is performed in the rest frame wavelength range 4150–6280 \AA , except two narrow windows around H γ and He I $\lambda 5876$. The two lines are not blended with the major part of Fe II emission, and their study is beyond the scope of the present paper. We keep them out of the fitting to avoid introducing too many unnecessary parameters. The observed spectra in the fitting windows are plotted in green, while those left out of the fitting are in black. The fitting includes the following components: (1) a single power law, (2) Fe II emission, (3) host galaxy. These three components, which when combined together forms the pseudo-continuum¹⁰, are plotted in blue. (4) H β emission line plotted in magenta. (5) Broad He II $\lambda 4686$ emission line plotted in cyan. (6) Narrow emission lines plotted in orange, including [O III] $\lambda\lambda 4959, 5007$, He II $\lambda 4686$, He I $\lambda 4471$, and several coronal lines. The summed model is plotted in red. The bottom panel shows the residual spectrum. Note that, although He I $\lambda 5876$ is not in the fitting window, its profile is well recovered after removing the Na I $\lambda\lambda 5890, 5896$ (Na D) absorption lines from the host galaxy.

Limited by the signal-to-noise ratio (S/N) for the individual-night spectra, there are degeneracies between several pairs of spectral components, including: (a) the AGN power-law continuum and the host galaxy; (b) Fe II emission and the broad He II line; (c) Fe II emission and the coronal lines. Thus, we first fit the high-S/N *mean spectrum* with all parameters set free. We then fit each individual-night spectrum with the values of some parameters fixed to those obtained from the fitting of the mean spectrum. The details of each spectral component, and the fitting parameters, are described in the following subsections.

3.1.1. AGN Power-law Continuum

A single power law is used to describe the featureless AGN continuum. It has two parameters: the flux density at 5100 \AA (F_{AGN}), and the spectral index (α , defined as $f_\lambda \propto \lambda^\alpha$). There is some degeneracy between the power-law continuum and the host galaxy. A larger α or a higher-flux galaxy (F_{gal}) both make the total spectrum redder (note that the unphysical change in the color of the observed spectrum caused by weather or differential atmospheric refraction is avoided in our observation, as our flux calibration by the comparison star provides differential spectrophotometry in each wavelength bin of the spectrum; see Section 2.2).

For our observations, we find that the *relative flux* of the galaxy component is the main reason for the change in the total-spectrum slope. Figure 1 illustrates this point. The right panel shows the spectrum of Mrk 382 taken at JD 2456299, just one day after the date of the spectrum shown in the left panel. Apparently, the flux at 5100 \AA is $\sim 30\%$ higher than the day before, and the color is redder. However, the difference between the V -band magnitudes of the two nights is only ~ 0.01 mag. We have therefore adopted an approach based on the assumption that the absolute flux of the host must be constant but the relative flux inside the slit can vary depending on the observing conditions. This is illustrated in detail in Appendix A. The conclusion about the AGN continuum is in line with several, but not all studies discussing the relation between α and luminosity in AGNs. Most recently, Zhang (2013) investigated this issue using the reverberation mapping data of the 17 quasars from Kaspi et al. (2000). They found no strong dependence of α on the variability of the luminosity. Thus, in the fitting of each individual-night spectrum, we fix the value of α to agree with the best fit to the mean spectrum, and let F_{AGN} and F_{gal} free. Comparing the left and right panels of Figure 1, only the galaxy component changes. In this way, the resultant F_{AGN} light curve matches the V -band light curve well (see Appendix A). Our fitting is consistent with no changes in spectral index as a function of luminosity.

3.1.2. Fe II Emission

There are several optical Fe II templates available in the literature. Among them, two templates, from Boroson & Green (1992) and Véron-Cetty et al. (2004), are most widely used, both constructed from the spectrum of the NLS1 galaxy I Zw 1. Barth et al. (2013) find that the template from Véron-Cetty et al. (2004) yields inconsistent He I emission lines; significant broad He I $\lambda 4922$ and $\lambda 5016$ emission lines are needed while He I $\lambda 4471$ is constrained to have zero flux by the fitting. We compared these two templates and found that the one from Boroson & Green (1992) gives better fitting as judged by the smaller reduced χ^2 . No broad He I $\lambda 4922$ and $\lambda 5016$ emission lines are needed, which is consistent with the zero flux of He I $\lambda 4471$. Introducing the two broad He I lines will add more parameters to the fit and will introduce additional degeneracy between He I $\lambda 4922$ and H β . Given this, we chose the Fe II template from Boroson & Green (1992) in this paper.

The Fe II template is convolved with a Gaussian function to be scaled, broadened, and shifted (see Hu et al. 2008, for details). Three parameters, the flux (F_{Fe}), the full width at half-maximum (FWHM_{Fe}), and shift (V_{Fe}), are used for Fe II emission in the fitting. We let all the three parameters to be free in the fitting of each individual-night spectrum. Note that, F_{Fe} is defined as the flux of the integrated Fe II emis-

⁹ <http://ned.ipac.caltech.edu/>

¹⁰ Note that the pseudo-continuum here is not defined in the ordinary way, in which the host galaxy component is not included.

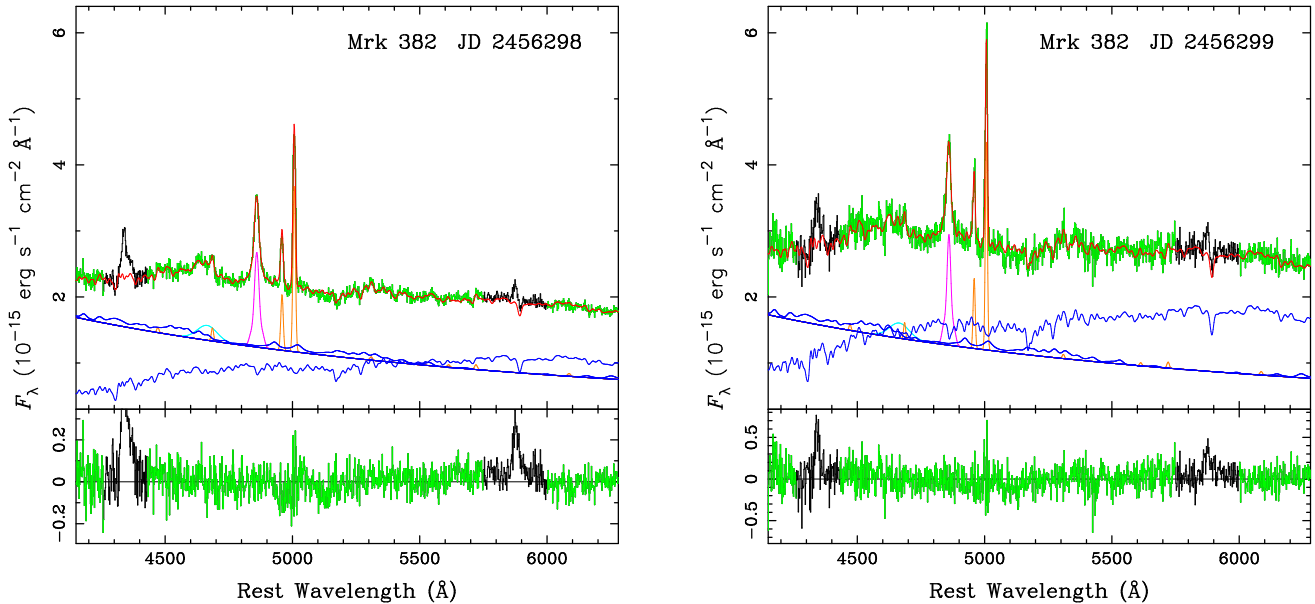


Figure 1. Individual-night spectra and multi-component model fitting for Mrk 382 taken at JDs 2456298 (left) and 2456299 (right). For each night, the top panel shows the Galactic extinction and redshift corrected spectrum (green or black for the parts in/out of the fitting window), and best-fit model (red). The model includes a pseudo-continuum (blue, composed by AGN power-law continuum, Fe II emission, and host galaxy) and several emission lines (H β in magenta, broad He II λ 4686 in cyan, and narrow emission lines in orange). The bottom panel shows the residuals. Note the large change in the host galaxy intensities for the two successive nights, which is not real but caused by our method of observation and calibration (see Appendix A for details).

sion between 4434 and 4684 Å from the best-fit Fe II model, following Boroson & Green (1992).

3.1.3. The H β Line

The spectral resolution of our spectra is rather low (~ 500 km s $^{-1}$), and in addition our objects are selected to have narrow H β emission lines. Thus, it is hard to decompose the H β emission line and remove the narrow component that comes from the narrow-line region. Considering that the contribution of the narrow component is weak and supposed to be constant over reverberation timescales (Peterson et al. 2013), we treat the entire H β emission line as one component. The entire H β profile is modeled by a Gauss-Hermite function (van der Marel & Franx 1993). All the five parameters of the Gauss-Hermite function are set free in the fitting of each individual-night spectrum. The flux of the line ($F_{H\beta}$) is calculated from the best-fit model.

3.1.4. Narrow Emission Lines

Besides the strong [O III] $\lambda\lambda$ 4959, 5007, there are many other narrow emission lines in the wavelength range of our fit spectrum (vanden Berk et al. 2001). We identify narrow He II λ 4686, He I λ 4471, and several high-ionization forbidden coronal lines. In some objects, these narrow lines are so strong that their contamination is non-negligible to the Fe II measurement. Figure 2 shows an individual-night spectrum of Mrk 335 and our fit. The strong coronal lines include in this case [Fe VII] λ 5158, [Fe VI] λ 5176, [N I] λ 5199, [Ca V] λ 5309, [Fe VII] λ 5721, and [Fe VII] λ 6086. Adding these lines significantly improve the fit.

The intensities of the narrow lines differ from one object to the next. For each object, we first identify narrow lines in the mean spectrum by testing the goodness of fit. Only lines that are identified in the mean spectrum are included in the fitting of individual-night spectra. Each narrow emission line is modeled by a Gaussian. These lines are coming from the narrow-line region and hence do not vary on the campaign

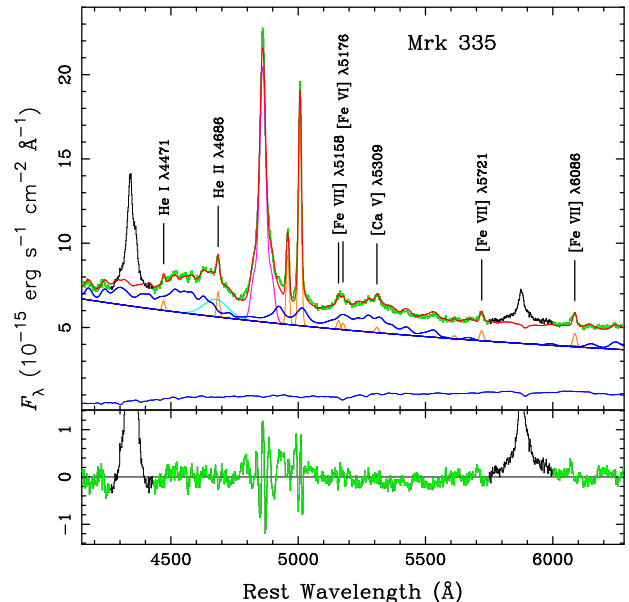


Figure 2. An example of individual-night spectrum and model fitting for Mrk 335. The spectrum, model, and residuals are plotted in the same manner as that in Figure 1. Note the strong narrow He II and coronal lines labeled by ion and wavelength.

time scale. Thus, we constrain them to have the same velocity width and shift with those of the [O III] λ 5007 line. The flux ratio relative to [O III] λ 5007 is also kept constant, as given by the best fit to the mean spectrum (the flux ratio of [O III] λ 4959 to λ 5007 is fixed to the theoretical value of 1/3), in order to avoid the degeneracy between these lines and Fe II. Only the flux, velocity width, and shift of [O III] λ 5007 are set free.

3.1.5. Broad He II Emission Line

The broad He II $\lambda 4686$ emission line is strong in the spectrum of some objects in our sample. Figure 2 shows an example. The line, plotted in cyan, is much broader than $H\beta$, and strongly blueshifted. Such a line profile is common for high-ionization lines in NLS1s and consistent with that of the ultraviolet (UV) He II $\lambda 1640$ line in SDSS spectra (Richards et al. 2011). It is even more prominent in the root-mean-square (rms) spectra of our objects, indicating large variability similar to the results in previous He II reverberation mapping studies (e.g., Bentz et al. 2010; Barth et al. 2011; Grier et al. 2012).

The broad He II line is heavily blended with Fe II emission. The high-ionization lines in AGN are often asymmetric (Richards et al. 2011), but there is no other high-ionization line in the wavelength range of our spectra to constrain the profile of He II line. We first fit the line profile in the mean spectrum using a single Gaussian. We then kept the width and the shift in the individual-night spectra but leave the line intensity as a free parameter.

The intensity variation of the He II lines in our sample will be discussed in a forthcoming publication. Here we only note that the procedure described above seems to be consistent with the observations, and, in general, the lag of this line is much shorter than the $H\beta$ lag.

3.1.6. Host Galaxy

Following Barth et al. (2013), we use single simple stellar population models from Bruzual & Charlot (2003) as templates for the galaxy component. For most objects in our sample, the instantaneous-burst model with an age of 11 Gyr and solar metallicity ($Z = 0.02$) provided sufficiently good fit to the mean spectrum and consistent flux ratio compared with the measured *Hubble Space Telescope* (*HST*) images (see Papers I and II). In a few cases (Mrk 335, Mrk 142, and Mrk 42), this template gives a flux that is much larger than that derived from the *HST* image. The template with 11 Gyr and $Z = 0.05$ provides better results and was adopted in these cases.

Like the Fe II template, the galaxy template is also convolved with a Gaussian to be scaled, broadened, and shifted. As described previously, and detailed in Appendix A, the relative flux F_{gal} is free to vary in the fitting of individual-night spectra.

3.2. Fitting Results

Table 1 lists the values of the parameters fixed in the fitting of individual-night spectra for all the objects in our sample. Columns (5) to (12) list the narrow emission lines included in the fits. As explained, their velocity widths and shifts are constrained to be the same with those of the [O III] $\lambda 5007$ line while the relative intensity ratios are kept as measured from the mean spectrum. The last column gives the galaxy template used. In the table, a blank entry means that spectral component is not included for the object.

Figure 3 shows examples of fittings to individual-night spectra for the eight objects not presented so far. The notations and colors are as the same as those in Figure 1 for Mrk 382. Notes on two objects with unusual treatments are as follows.

IRAS 04416+1215. This object has the highest redshift (0.089) in our sample. From the images taken for slit centering, the point spread function of the object is as broad as that of the comparison star, meaning that there is a negligible galaxy contribution. For this object, the comparison star

is fainter than the AGN, especially in the red part. We found that the shape of the spectrum of this object is not as well calibrated by the comparison star as in the other objects. Thus, we fit in a relatively narrow wavelength window (4430–5550 Å), but covering the two bumps of Fe II emission on either side of $H\beta$. We also let the spectral index α of the AGN power-law continuum free to vary in individual-night spectra to compensate for the difference in spectral shape caused by the calibration. As shown in Figure 3, the spectrum can be fitted well by including only a power law, Fe II emission, $H\beta$, [O III], and a few narrow lines.

IRAS F12397+3333. As discussed in Paper I, the spectrum of this AGN is probably affected by host galaxy extinction. The observed spectra (see Figure 4 of Paper I for an example) have a very red color, and are badly fitted by our spectral model. We perform an extinction correction after deredshifting, assuming the Galactic extinction law and $A_V = 1.44$ mag estimated from the Balmer decrement (see details in Paper I). This dereddened spectrum is fit well with a typical spectral index as shown in Figure 3.

3.3. Line-profile Measurements

For each individual-night spectrum, the fluxes, FWHMs, and velocity shifts (with respect to [O III]) of Fe II and $H\beta$ are calculated from the best-fit model. The means of these properties are considered to be the measurements of the line profile, except for the width of $H\beta$ ($\text{FWHM}_{H\beta}$; see below). The standard deviations on those means are used as the uncertainties.

$\text{FWHM}_{H\beta}$ is underestimated in the fitting, as we do not include the narrow component of $H\beta$ in our model (see Section 3.1.3). Thus, we use a different method to estimate this width. We add a Gaussian to our model to represent the narrow $H\beta$ component. The velocity width and shift are constrained to be the same as those of [O III]. We then fit the mean spectra twice, once assuming the flux of the narrow $H\beta$ line is 10% of the flux of [O III] $\lambda 5007$ and once assuming a flux ratio of 0.2. The width of the broad $H\beta$ obtained with flux ratio set to 0.1 is adopted as the $\text{FWHM}_{H\beta}$. The uncertainty is obtained from the fit with a flux ratio set to 0.2 and the original fit that assumed no narrow $H\beta$. This method essentially resembles the one used in Papers I and II, while the spectral model here is more sophisticated.

Table 2 lists the measurements of the 10 objects. The instrumental broadening ($\text{FWHM} \sim 500 \text{ km s}^{-1}$, Section 3.1.3) has been taken into account in the listed FWHMs. Note that the $H\beta$ of IRAS 04416+1215 has large velocity shift with respect to [O III] $\lambda 5007$, and its profile shows no feature of a narrow component with the same shift of [O III]. Adding a narrow component makes the width of the broad $H\beta$ even narrower. Thus, the $\text{FWHM}_{H\beta}$ of IRAS 04416+1215, as other properties, was obtained from the measurements of individual-night spectra.

3.4. Light-curve Measurements

Our fitting successfully reduces the scatter in the light curves due to the influence of the host galaxy contamination; thus, F_{AGN} represents the real AGN continuum much better than the simply integrated 5100 Å flux (F_{5100}), as shown in Appendix A. The light curves of the emission lines are also generated directly from the best-fit values of the corresponding parameters obtained from the fits of individual-night spectra. The errors of the fluxes given by the fitting are not large

Table 1
Parameters Fixed in the Fitting of Individual-night Spectrum

Object	Power Law α ($f_\lambda \propto \lambda^\alpha$)	Broad He II $\lambda 4686$		Narrow Emission Lines								Galaxy model
		FWHM ^a (km s ⁻¹)	Shift (km s ⁻¹)	He I $\lambda 4471$	He II $\lambda 4686$	[Fe VII] $\lambda 5158$	[Fe VI] $\lambda 5176$	[N I] $\lambda 5199$	[Ca V] $\lambda 5309$	[Fe VII] $\lambda 5721$	[Fe VII] $\lambda 6086$	
(1)	(2)	(3)	(4)	(5)	(6)	(7)	(8)	(9)	(10)	(11)	(12)	(13)
Mrk 335	-1.45	7082	-620	0.042	0.115	0.043	0.032	...	0.028	0.057	0.079	11Gyr_z05
Mrk 1044	-2.01	5161	-942	0.216	...	0.117	0.219	0.205	0.225	11Gyr_z02
IRAS 04416+1215	free ^b	0.095	0.042
Mrk 382	-1.96	5797	-1322	0.028	0.074	0.021	0.033	0.021	11Gyr_z02
Mrk 142	-2.11	4824	-757	0.041	0.131	0.055	0.116	0.082	0.095	11Gyr_z05
MCG +06-26-012	-0.84	5191	-927	0.063	0.096	0.046	0.061	11Gyr_z02
IRAS F12397+3333 ^c	-2.28	5506	-334	...	0.034	0.013	...	0.018	...	0.008	0.010	11Gyr_z02
Mrk 42	-0.70	1472	-55	0.069	0.093	11Gyr_z05
Mrk 486	-0.76	4877	-724	...	0.171	0.027	0.067	0.050	0.140	11Gyr_z02
Mrk 493	-0.91	4054	-1580	0.132	0.261	11Gyr_z02

Note. — Fixed parameters in the fitting of individual-night spectra. Columns (2) to (4) list the absolute values of the parameters. Columns (5) to (12) list the relative intensity ratios with respect to [O III] $\lambda 5007$ for the narrow emission lines. Column (13) lists the galaxy template from Bruzual & Charlot (2003). ... means that the component is not included in the fitting for the specific object.

^a The FWHMs listed are after instrumental broadening correction.

^b The spectral index of the power-law continuum is free to vary in the fitting of the IRAS 04416+1215 spectra, see text for details.

^c Intrinsic host galaxy extinction is assumed in the fitting of IRAS F12397+3333. See text for details.

Table 2
Line-profile Measurements

Object	Fe II			H β		
	Flux (10 ⁻¹⁵ erg s ⁻¹ cm ⁻²)	FWHM (km s ⁻¹)	Shift (km s ⁻¹)	Flux (10 ⁻¹⁵ erg s ⁻¹ cm ⁻²)	FWHM ^a (km s ⁻¹)	Shift (km s ⁻¹)
Mrk 335	253 \pm 9	1947 \pm 143	49 \pm 37	661 \pm 22	2096 \pm 170	-1 \pm 16
Mrk 1044	369 \pm 11	866 \pm 25	76 \pm 10	380 \pm 16	1178 \pm 22	12 \pm 12
IRAS 04416+1215	292 \pm 9	1313 \pm 50	496 \pm 21	149 \pm 4	1522 \pm 44 ^b	241 \pm 29
Mrk 382	27 \pm 4	1326 \pm 234	13 \pm 115	39 \pm 2	1462 \pm 296	-44 \pm 35
Mrk 142	87 \pm 5	1512 \pm 69	-25 \pm 37	78 \pm 5	1588 \pm 58	-101 \pm 28
MCG +06-26-012	41 \pm 4	1155 \pm 70	-21 \pm 41	41 \pm 4	1334 \pm 80	-29 \pm 23
IRAS F12397+3333	550 \pm 28	1748 \pm 78	36 \pm 40	405 \pm 18	1802 \pm 560	-50 \pm 26
Mrk 42	67 \pm 3	787 \pm 16	105 \pm 19	57 \pm 2	802 \pm 18	87 \pm 19
Mrk 486	186 \pm 5	1790 \pm 88	95 \pm 33	346 \pm 12	1942 \pm 67	-46 \pm 9
Mrk 493	102 \pm 3	780 \pm 9	171 \pm 9	92 \pm 3	778 \pm 12	126 \pm 13

Note. — Fluxes, FWHMs, and velocity shifts of Fe II and H β . Except for the H β FWHMs, the listed values are the means and standard deviations obtained from the measurements of individual-night spectra. All listed FWHMs include a correction due to instrumental broadening. The velocity shifts are with respect to [O III].

^a H β FWHMs are estimated from the mean spectrum of each object taking into account the narrow H β component, as explained in the text.

^b H β FWHM for IRAS 04416+1215 is obtained from individual-night spectra. See text for details.

enough to account for the scatter in the fluxes of successive nights, an additional systematic error is estimated for each light curve (as in Paper I). This systematic error is added in quadrature to the fitting error for the calculations of variability amplitudes and time lags below. Note that our treatment is different from that of Barth et al. (2013), who measured the light curve of H β by integrating the continuum-subtracted spectra.

4. LIGHT-CURVE ANALYSIS AND RESULTS

The left columns of Figure 4 and Figure 5 show the light curves of F_{AGN} , $F_{\text{H}\beta}$, and F_{Fe} for nine objects with reliable lag measurements, and the remaining one (Mrk 42), respectively. In this section, we will calculate the variability amplitudes and the reverberation lags for the H β and Fe II emission lines. We then compare the H β time lags with those presented in Papers I and II.

4.1. Variability Amplitudes

We use the quantity F_{var} defined in Rodríguez-Pascual et al. (1997) to represent the variability amplitude. This quantity is

an estimate of the intrinsic variability over the errors. The uncertainties are calculated following Edelson et al. (2002). The results for Fe II and H β are listed in Table 3. For the variability amplitude ratio of Fe II to H β , the range is from about 0.6 (Mrk 486) to 1.2 (Mrk 42), except for Mrk 382 which has the largest host galaxy contamination. On average (except for Mrk 382), the Fe II value is about 10% smaller, consistent with previous results (e.g., Vestergaard & Peterson 2005; Barth et al. 2013).

4.2. Reverberation Lags

The time lags between the AGN continuum variations (F_{AGN}) and the emission lines (F_{Fe} and $F_{\text{H}\beta}$) are measured from the cross-correlation functions (CCFs) for the relevant light curves. We use the interpolation cross-correlation function (ICCF; Gaskell & Sparke 1986; Gaskell & Peterson 1987; White & Peterson 1994) method to calculate the CCF, and adopt the centroid of the CCF, above 80% of the peak value (r_{max}) as the time lag (Koratkar & Gaskell 1991; Peterson et al. 2004). The uncertainty in the time lag mea-

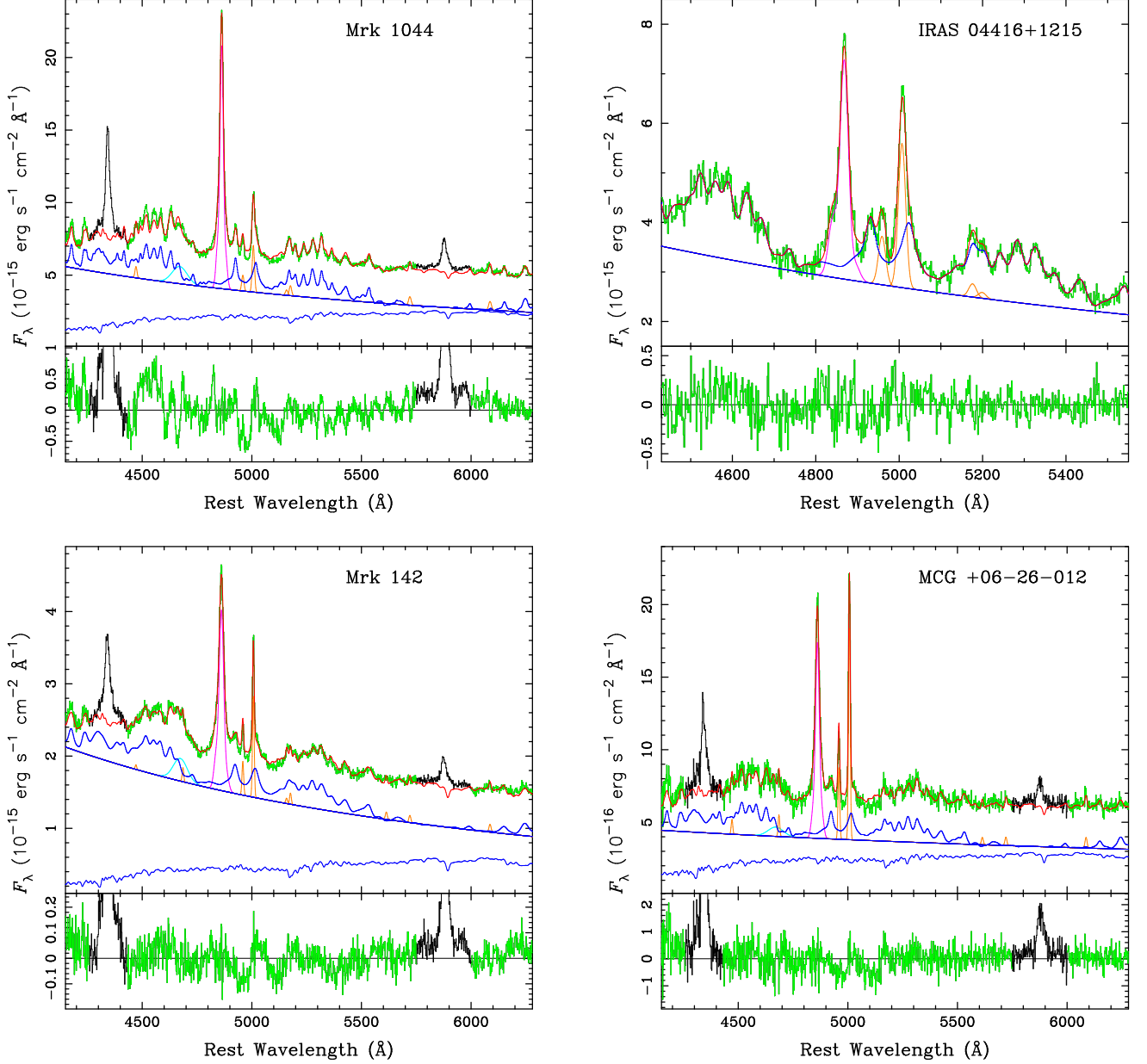


Figure 3. Examples of individual-night spectra and model fittings for the other eight objects. For each object, the spectrum, model, and residuals are plotted in the same manner as those in Figure 1.

Table 3
Variability Amplitudes

Object	F_{var}	
	Fe II	H β
Mrk 335	3.1 ± 0.3	3.0 ± 0.3
Mrk 1044	2.6 ± 0.3	3.7 ± 0.4
IRAS 04416+1215	2.1 ± 0.3	2.0 ± 0.3
Mrk 382	11.5 ± 1.2	4.1 ± 0.4
Mrk 142	5.5 ± 0.5	6.6 ± 0.5
MCG +06-26-012	8.1 ± 1.2	9.2 ± 1.2
IRAS F12397+3333	4.4 ± 0.6	4.1 ± 0.5
Mrk 42	3.6 ± 0.7	2.9 ± 0.4
Mrk 486	2.0 ± 0.5	3.4 ± 0.4
Mrk 493	2.1 ± 0.7	3.1 ± 0.5

Note. — The listed values are in percentage.

urement is estimated from the cross-correlation centroid distribution (CCCD) given by random subset selection/flux randomization Monte Carlo realizations (Maoz & Netzer 1989; Peterson et al. 1998).

All objects in our sample, except for Mrk 42, have reliable time lag measurements for both Fe II and H β . The right column of Figure 4 show the results of the CCF analysis. For each object, the top-right panel shows the autocorrelation function (ACF) of the F_{AGN} light curve, which is shown in the top-left panel. The two lower panels in the right column show the CCFs (in black) for H β (middle-right) and Fe II (bottom-right) with respect to F_{AGN} light curves. The blue histograms are the corresponding CCCDs. Most CCCDs have a rather symmetric profile, except those for IRAS 04416+1215.

Table 4 lists the time lags of Fe II (τ_{Fe}) and H β ($\tau_{\text{H}\beta}$), their uncertainties, and the corresponding r_{max} , for the nine objects with reliable lag measurements. The listed time lags and un-

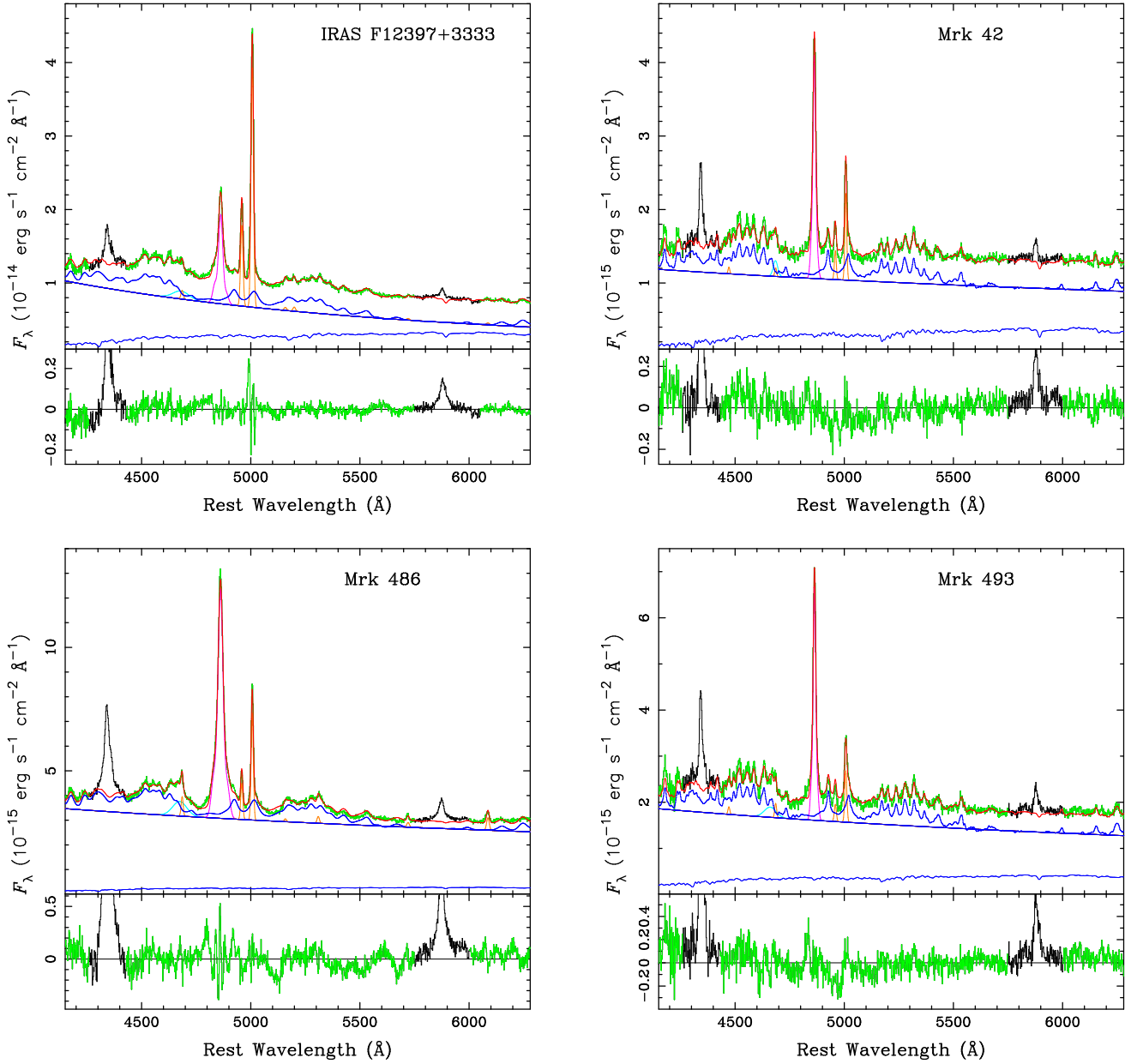


Figure 3. Continued.

certainties are in the rest frame after time-dilation correction. Both time lags for IRAS 04416+1215 have uncertainties of highly unequal upper and lower limits, as the sequence of their asymmetric CCCDs. For other objects, the time lags are well determined by the single-peak CCFs with high r_{\max} and symmetric, narrow CCCDs.

The detection rate of Fe II time lag in our sample is extremely high (9 in 10), compared with previous reverberation-mapping experiments. This is mainly attributed to the common feature of strong Fe II emission in the SEAMBH sample, the high-cadence observation, and sophisticated spectral fitting. The failure to obtain reliable τ_{Fe} and $\tau_{\text{H}\beta}$ in Mrk 42 is caused by the F_{AGN} light curve, which has large scatter and no clear structure (see Figure 5). However, the light curves of F_{Fe} and $F_{\text{H}\beta}$ show hints for a similar structure which, unfortunately, is not enough to establish a time lag.

The clear reverberation of the Fe II emission in response to

Table 4
Time Lag Measurements

Object	Fe II		H β	
	r_{\max}	τ_{Fe}	r_{\max}	$\tau_{\text{H}\beta}$
Mrk 335	0.48	$26.8^{+2.9}_{-2.5}$	0.70	$8.7^{+1.6}_{-1.9}$
Mrk 1044	0.48	$13.9^{+3.4}_{-4.7}$	0.62	$10.5^{+3.3}_{-2.7}$
IRAS 04416+1215	0.61	$12.6^{+16.7}_{-6.7}$	0.60	$13.3^{+13.9}_{-1.4}$
Mrk 382	0.40	$23.8^{+6.0}_{-6.0}$	0.47	$7.5^{+2.9}_{-2.0}$
Mrk 142	0.78	$7.6^{+6.4}_{-2.2}$	0.84	$7.9^{+1.2}_{-1.1}$
MCG +06–26–012	0.86	$22.4^{+9.3}_{-6.0}$	0.92	$24.0^{+8.4}_{-4.8}$
IRAS F12397+3333	0.63	$10.6^{+7.0}_{-1.9}$	0.71	$9.7^{+5.8}_{-1.3}$
Mrk 486	0.77	$17.3^{+5.8}_{-3.7}$	0.79	$23.7^{+7.5}_{-2.7}$
Mrk 493	0.63	$11.9^{+3.6}_{-6.5}$	0.81	$11.6^{+1.2}_{-2.6}$

Note. — Time lags are in the rest frame, and in units of days.

the continuum supports the hypothesis that the Fe II emission

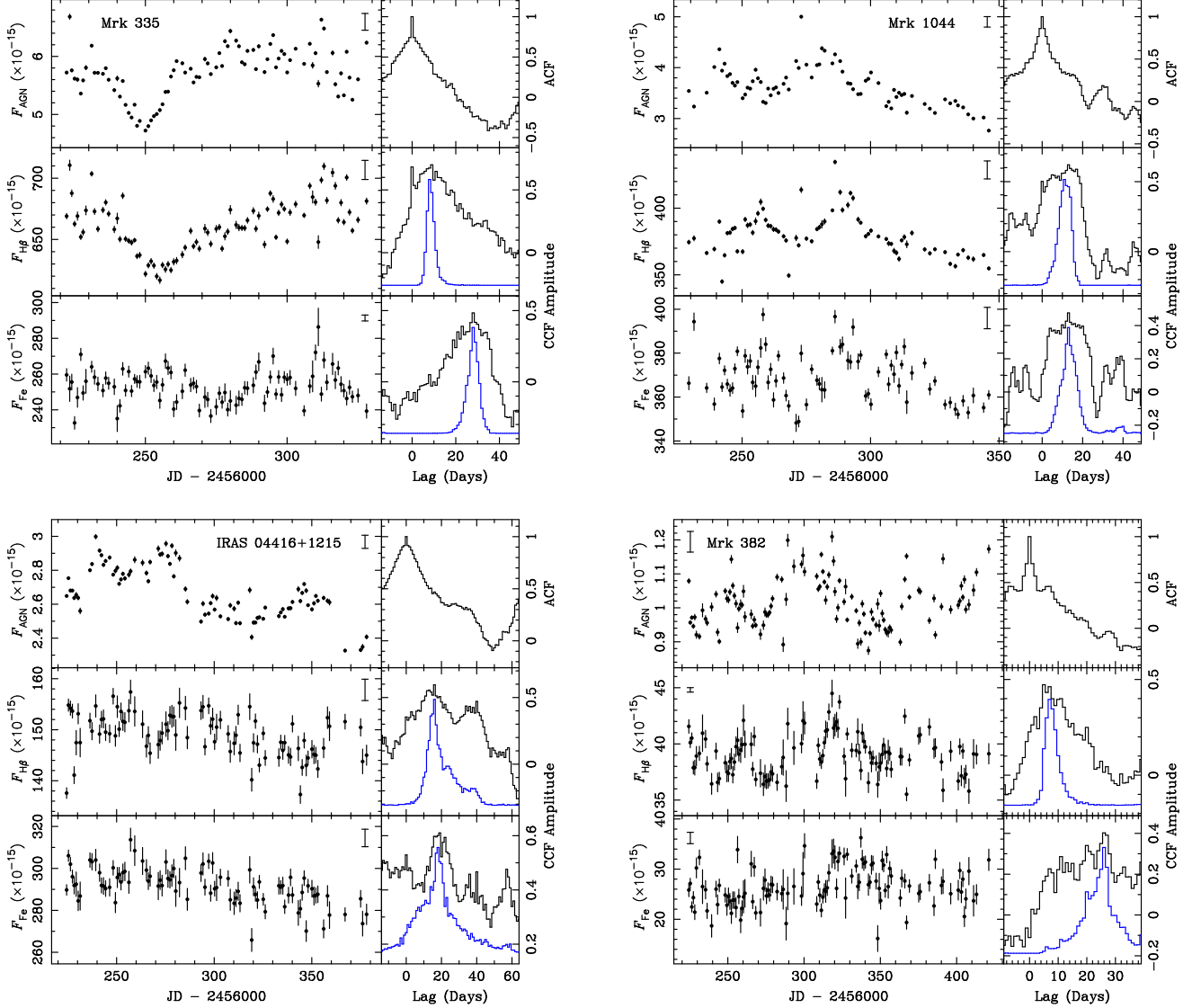


Figure 4. Light curves and cross-correlation functions for the nine objects with reliable time lag measurements. For each object, the left column show the light curves of the AGN (top-left), $H\beta$ (middle-left), and Fe II (bottom-left). The error bar of each flux point is only the fitting error. For each light curve, an additional systematic error is estimated from the scatter in the fluxes of successive nights, and plotted as the error bar with terminals in the corner of the panel. The right column show the autocorrelation function of the AGN light curve (top-right), cross-correlation functions for $H\beta$ (middle-right) and Fe II (bottom-right) with respect to the AGN continuum. The blue histograms in the middle-right and bottom-right panels are the corresponding cross-correlation centroid distributions.

originates from photoionized gas in the BLR. The high detection rate indicates that this is prevalent in NLS1, which are AGNs with high $L_{\text{bol}}/L_{\text{Edd}}$. It is possible that the origin of Fe II emission in AGNs with low $L_{\text{bol}}/L_{\text{Edd}}$ is different, but there is little evidence to support this claim. In fact, Barth et al. (2013) has already detected the reverberation of Fe II in two broad-line Seyfert 1 galaxies with $H\beta$ widths of $\text{FWHM} \gtrsim 4000 \text{ km s}^{-1}$ and much lower $L_{\text{bol}}/L_{\text{Edd}}$. Comparing the time lags of Fe II and $H\beta$, along with their velocity widths, provides some hints about the location and geometries of the two emission regions. We will discuss these ideas in Section 5.2 below.

4.3. $H\beta$ Lag Comparison

In Paper I and II, the reported time lags of $H\beta$ are obtained from the light curves measured by the more traditional integration method, without taking into account the contamination by the host galaxy and the narrow emission lines. Figure

6 shows a comparison between the previously reported $\tau_{H\beta}$ based on the integration method and the new results given by the fitting method reported here. The dashed diagonal line denotes the 1:1 ratio and the region between the two dotted lines gives the 0.1 dex deviation from the line. For seven out of nine objects, the differences between $\tau_{H\beta}$ given by the two methods are less than 0.1 dex. The two exceptions are IRAS 04416+1215 and Mrk 1044. In Paper II we show that using the integration method, we cannot obtain a significant $\tau_{H\beta}$ for IRAS 04416+1215. The lag for Mrk 1044 reported in that paper is about a factor 2 shorter than obtained here, with a very large uncertainty ($4.8_{-3.7}^{+7.4}$). This value is consistent with the new one presented here within the uncertainties. In addition, the uncertainty on $\tau_{H\beta}$ in Mrk 493 given by the integration method is very large with a negative lower limit ($12.2_{-16.7}^{+3.5}$). The fitting method yields much smaller uncertainty with basically the same $\tau_{H\beta}$. This is a direct result of the much smoother $H\beta$ light curve of Mrk 493 given by the

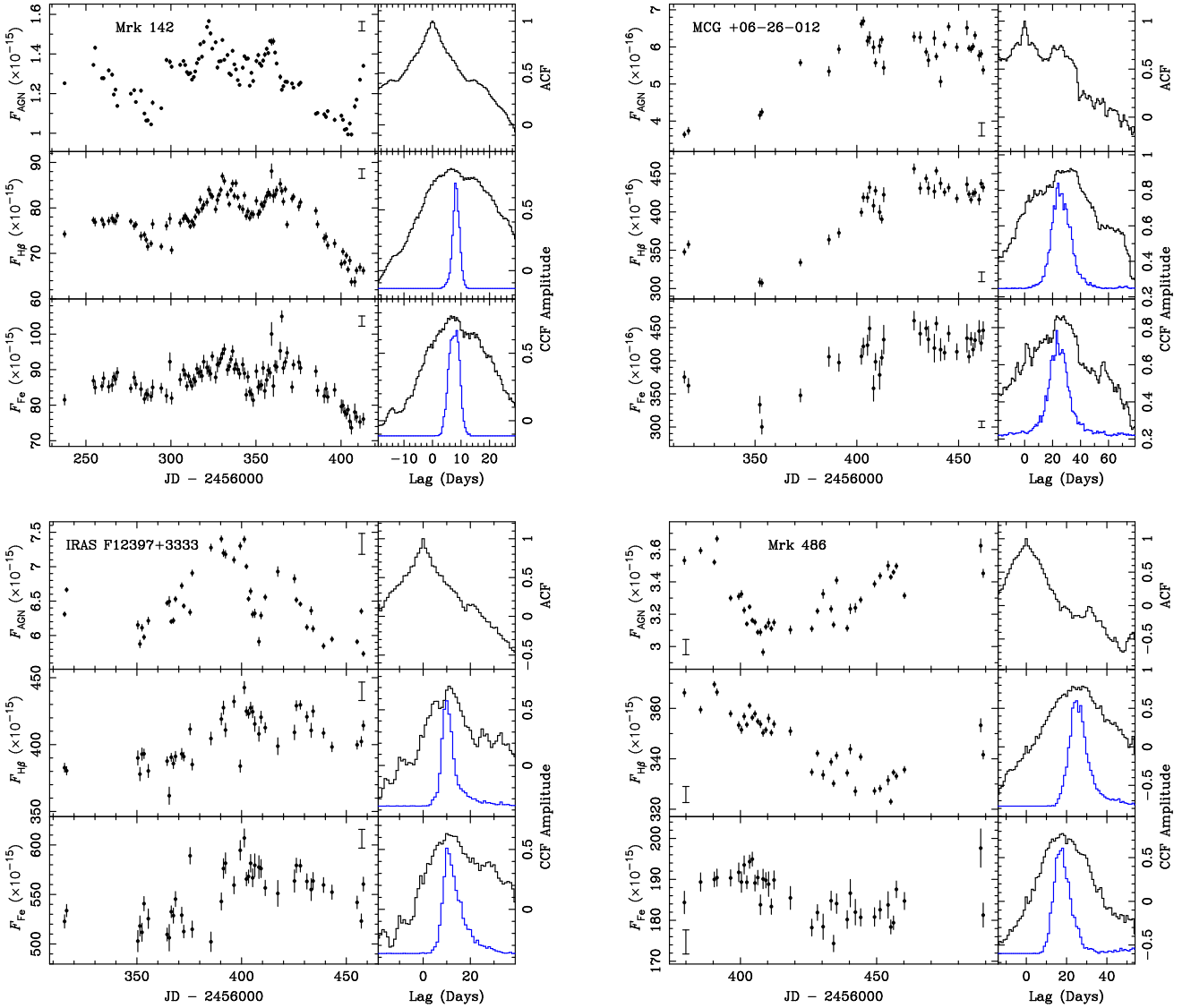


Figure 4. Continued.

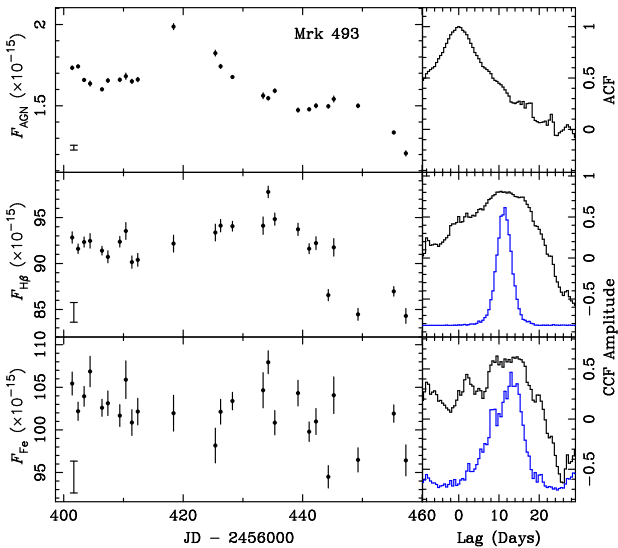


Figure 4. Continued.

fitting method (see Figure 4, and also Figure 2 of Paper II). Thus, the time lags of $\text{H}\beta$ given by the two methods are consistent with each other and $\tau_{\text{H}\beta}$ is better defined by the fitting procedure in some of the cases.

5. DISCUSSION

5.1. The Radius–Luminosity Relationship for Fe II

A simple theoretical expectation based on photoionization is that $R_{\text{BLR}} \propto L^\alpha$ with $\alpha \sim 0.5$. The $R_{\text{BLR}}-L$ relation for $\text{H}\beta$ has been compared with such predictions in several earlier publications (e.g., Kaspi et al. 2000; Bentz et al. 2009, 2013, and references therein). Regarding Fe II lines, Chelouche et al. (2014) provide a tentative $R_{\text{BLR}}-L$ relation for the first time, from a small inhomogeneous sample of six AGNs. Among them, two objects are reported by Barth et al. (2013) using the standard spectral fitting method, four others come from Rafter et al. (2013) and Chelouche et al. (2014) using the MCF scheme of Chelouche & Zucker (2013). Here, we revisit this issue by more than doubling the size of the sample by adding our nine newly measured sources. For a proper comparison with the Chelouche et al. (2014) results we

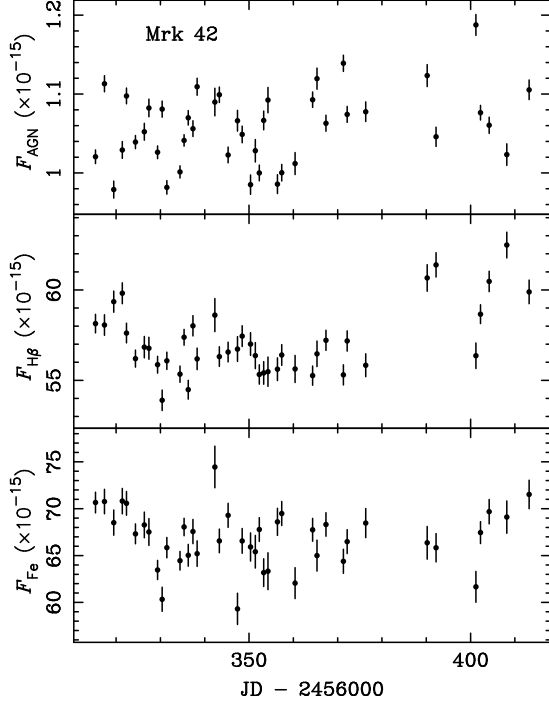


Figure 5. Light curves of the AGN (top panel), H β (middle), and Fe II (bottom) for Mrk 42. Note the similarity of the light curves of H β and Fe II.

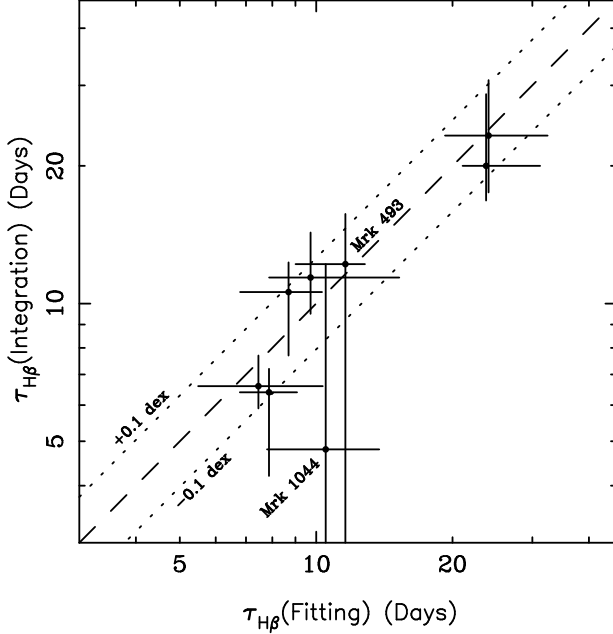


Figure 6. A comparison of the H β time lags obtained by simple integration (Papers I and II) with those obtained by fitting (this work). The differences are typically less than 0.1 dex (dotted lines) except for IRAS 04416+1215 (not plotted because its $\tau_{H\beta}$ cannot be defined by integration) and Mrk 1044 (very large uncertainty of the integration method). Mrk 493 also has very large uncertainty when measured by the integration method but the measured $\tau_{H\beta}$ are very similar.

used our best observed fluxes and uncertainty and a cosmology with $H_0 = 70 \text{ km s}^{-1} \text{ Mpc}^{-1}$, $\Omega_m = 0.3$, and $\Omega_\Lambda = 0.7$.

Figure 7 shows τ_{Fe} vs. the 5100 Å luminosity for the nine objects in our sample (black dots) alongside the earlier results (kindly provided by D. Chelouche). The green squares are those obtained by the MCF scheme (including three with

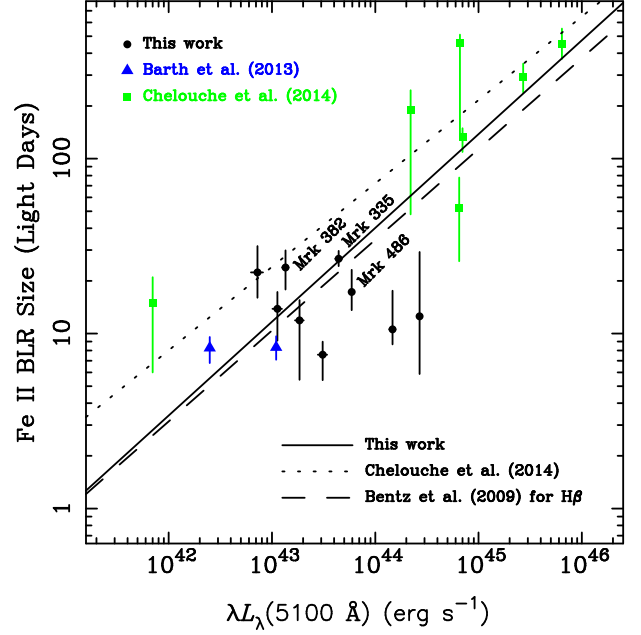


Figure 7. Fe II $R_{BLR}-L$ relation. The nine objects in our sample are plotted as black dots, the three objects with their names labeled have relatively large differences between $\tau_{H\beta}$ and τ_{Fe} . Measurements from previous studies are plotted as blue triangles and green squares (see text for details). The solid line is the fit to the entire data set. The dotted and dashed lines are the $R_{BLR}-L$ relations in Chelouche et al. (2014) for Fe II and Bentz et al. (2009) for H β , respectively.

insignificant results, see Figure 4 of Chelouche et al. 2014 for details). The blue triangles are the two objects from Barth et al. (2013) for which we used the centroid of the published CCFs for Fe II and the V-band light curves. Using the FITEXY method (Press et al. 1992) to fit all the 18 objects we find:

$$\log(R_{Fe \text{ II BLR}}) = (-22.0 \pm 1.1) + (0.54 \pm 0.02) \log(\lambda L_\lambda(5100 \text{ \AA})), \quad (1)$$

which is plotted in a solid line. This line deviates considerably from the relation presented in Chelouche et al. (2014) (shown in a dotted line), but close to that of Bentz et al. (2009) for H β (dashed line). This result is expected since most of the objects in our sample show roughly equal τ_{Fe} and $\tau_{H\beta}$ (see Table 4), except for three objects (Mrk 335, Mrk382, and Mrk486), while the previous studies have τ_{Fe} greater than $\tau_{H\beta}$. Our sample by itself shows no correlation at all between τ_{Fe} and the 5100 Å luminosity. This is not surprising given the relatively small range in luminosity considered by us and the fact that for this sample, the correlation between $\tau_{H\beta}$ and the continuum luminosity is also very weak. We suggest that this lack of correlation is related also to the large L_{bol}/L_{Edd} of the objects in our sample, a topic which we discuss in great detail in Paper IV (Du et al., submitted).

5.2. Comparison between Fe II and H β

As shown in Table 4, τ_{Fe} is roughly equal to $\tau_{H\beta}$ (counting the uncertainties in both lags) in six of our objects, longer in two (Mrk 335 and Mrk 382) and somewhat shorter in one (Mrk 486). A common feature of the three objects with unequal lags is the relatively low Fe II/H β intensity ratio. Figure 8 shows the plot of $\tau_{Fe}/\tau_{H\beta}$ vs. $F_{Fe}/F_{H\beta}$ (defined as R_{Fe}). The three objects with different time lags are labeled by their names and locate in the region of $R_{Fe} < 1$. The six other objects show $R_{Fe} > 1$. We also mark the approximate positions

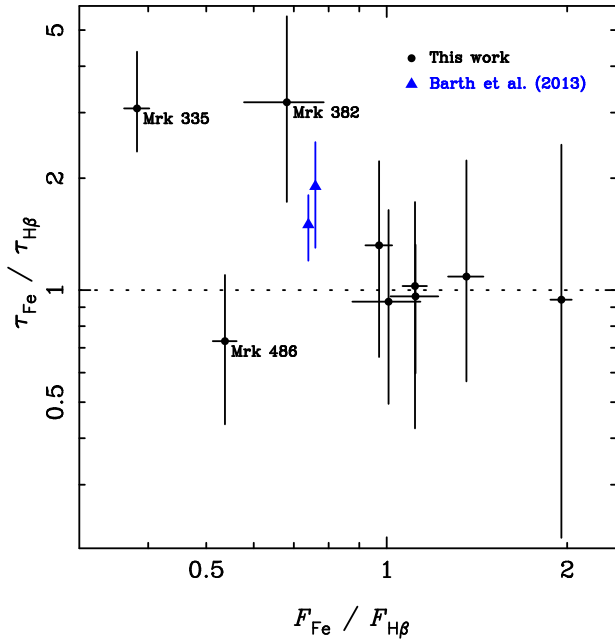


Figure 8. Time lag ratios of Fe II to H β vs. intensity ratios of Fe II to H β . Objects in our sample are shown as black dots. The three objects labeled by names have different time lags of Fe II and H β , and all have low intensity ratio of Fe II to H β . Blue triangles show the approximate positions of the two objects in Barth et al. (2013) (intensity ratios are estimated by eye). The two points are slightly shifted horizontally for clarity (See text for details.)

of the two objects measured by Barth et al. (2013).¹¹ Based on eye estimates of the published light curves shown in their paper, both objects have $R_{\text{Fe}} \sim 0.75$. Their positions in Figure 8 are marked around 0.75 (and horizontally shifted for clarity). They both have different time lags than H β and $R_{\text{Fe}} < 1$, consistent with the results of our sample.

We note, again, that our sample is highly biased toward AGNs with high $L_{\text{bol}}/L_{\text{Edd}}$ and thus high R_{Fe} . In an unbiased AGN sample, the fraction of sources with $R_{\text{Fe}} < 1$ is much larger (see, e.g., Figure 7 of Sulentic et al. 2000 and Figure 1 of Shen & Ho 2014). Hu et al. (2008) analysed the properties of a large number of low-redshift AGNs. They found that the velocity width of Fe II is systematically narrower ($\sim 3/4$) than that of H β , which may suggest, given Keplerian velocities, that in those sources τ_{Fe} is longer than $\tau_{\text{H}\beta}$. Our present sample contains only 10 sources which is too few to test, systematically, any of these ideas.

6. SUMMARY

We provide new Fe II measurements for 10 NLS1s and report statistically significant time lag measurements for nine of these sources. All the observed NLS1s are suspected to be SEAMBHs. This more than doubles the number of AGN showing measurable Fe II time lags. Our time lag measurements are based on high-cadence, high-S/N measurements at the Yunnan observatory, and on a new, sophisticated, fitting analysis that takes into account the uncertainties caused by the apparent flux change of the host galaxy and several narrow emission lines. We demonstrate, by a careful comparison with earlier measurements of $\tau_{\text{H}\beta}$, that the method can considerably improve the accuracy of the time lag measurement.

¹¹ The Fe II flux in Barth et al. (2013) is defined as the integrated flux of Fe II between 4400 and 4900 Å, while our definition refers to the range between 4434 and 4684 Å. For the Fe II template of Boroson & Green (1992), F_{Fe} defined here is about 3/4 that in Barth et al. (2013).

The main findings reported in this paper can be summarized as follows:

1. All 10 objects presented here show Fe II variations with an amplitude of a few to ten percent. On average, this is about 10% smaller than the variability of the H β line.
2. Reliable Fe II reverberation time lags with respect to the AGN continuum are detected in nine objects, confirming the suggestion that the Fe II emission originates from photoionized gas.
3. Combining the new reverberation mapping results with those in previous work, shows a clear radius–luminosity relationship for Fe II that is similar to the one for H β . However, our sample by itself shows no such correlation due to the large intrinsic scatter over a small luminosity range.
4. The difference in the time lags of Fe II and H β depends on the intensity ratio of Fe II to H β (R_{Fe}). The time lag of Fe II is roughly equal to that of H β in all the six objects with $R_{\text{Fe}} \gtrsim 1$. The Fe II time lag is longer in Mrk 335 and Mrk 382, those objects with $R_{\text{Fe}} < 1$, and shorter in Mrk 486 with $R_{\text{Fe}} < 1$.

We acknowledge the support of the staff of the Lijiang 2.4m telescope. Funding for the telescope has been provided by CAS and the People’s Government of Yunnan Province. This research is supported by the Strategic Priority Research Program – The Emergence of Cosmological Structures of the Chinese Academy of Sciences, grant No. XDB09000000, by the NSFC through NSFC-11173023, -11133006, -11233003, -11473002, and by Israel-China ISF-NSFC grant 83/13.

APPENDIX

A. HOST GALAXY FLUX CALIBRATION

Our flux calibration method provides the *relative* flux of the object with respect to that of the local comparison star. For two point sources kept in a line parallel to the slit, the fractions of light loss due to seeing, differential atmospheric refraction, and mis-centering are identical. Thus this method gives accurate relative flux calibration for the spectral components of the AGN, including the featureless power law (F_{AGN}) and the broad emission lines. This is not the case for the extended host galaxies whose flux relative to the comparison star inside the slit can vary much more due to seeing variations and mis-centering. In addition, different parts of the galaxy may be observed each time. As a result, the derived flux of the host galaxy is $F_{\text{gal}} = f_{\text{cal}} F_{\text{gal,abs}}$, where $F_{\text{gal,abs}}$ is the absolute flux (which is constant), and f_{cal} is a factor accounting for all the effects of varying observing conditions in the flux calibration procedure. f_{cal} could change from one exposure to the next, introducing an additional uncertainty into the integrated 5100 Å flux $F_{5100} = F_{\text{AGN}} + f_{\text{cal}} F_{\text{gal,abs}}$.

In Papers I and II, we estimated the flux of the host galaxies in the spectral extraction aperture using archival *HST* images for eight objects in our sample. The resultant relative fluxes, ($F_{\text{gal}}/F_{\text{AGN}}$), range from ~ 0.2 in Mrk 335 to $\gtrsim 1$ in Mrk 382. Thus, the apparent change of flux of the host galaxy is not negligible for those objects with strong host galaxy contribution. For Mrk 382, the measurement of the AGN continuum was badly affected by this uncertainty, which forced us to use

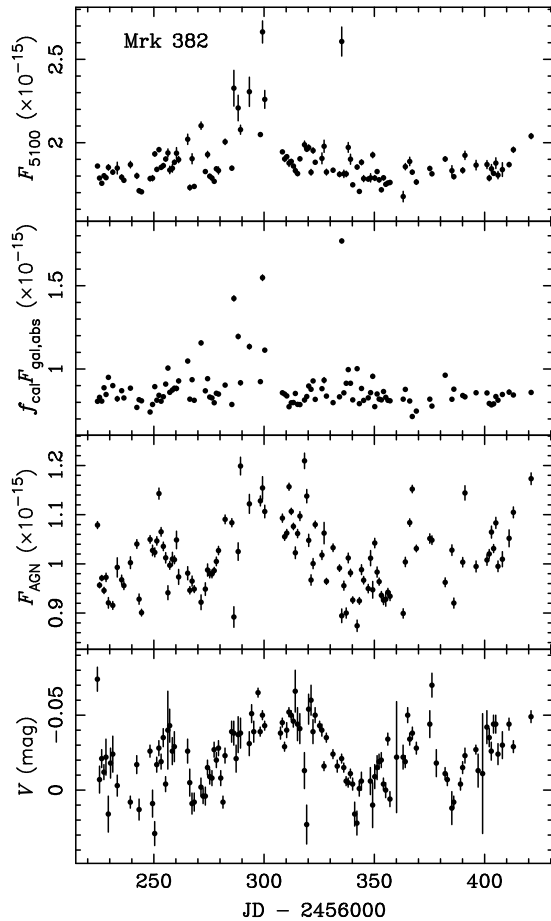


Figure 9. Light curves of the integrated 5100 Å flux (F_{5100} , top panel), fitted host galaxy ($f_{\text{cal}}F_{\text{gal,abs}}$ described in Appendix A, upper-middle panel), fitted AGN power-law continuum (F_{AGN} , lower-middle panel), and V -band magnitude (bottom panel, see also Paper II). Note that F_{5100} is heavily contaminated by the host whose apparent flux is varying by f_{cal} , and the F_{AGN} recovers, accurately, the intrinsic AGN variability as judged by a comparison with the V -band observations.

the V -band photometry instead. The new procedure adopted here (see the main text) enables us to solve for $f_{\text{cal}}F_{\text{gal,abs}}$ for each individual-night spectrum. The detailed fitting of the various spectral components considerably reduces the noise in the various line and continuum light curves. In particular, for Mrk 382, we can now recover the 5100 Å AGN continuum variations to a much better accuracy, which is evident by the good agreement with the V -band photometry.

The big improvements due to the spectral fitting procedure are shown in Figure 9, which provides more information on the process for Mrk 382. The top panel shows the light curve of F_{5100} , which is measured as in Papers I and II, except for the inclusion of Galactic extinction correction and de-redshifting. The scatter in this light curve is very large, and hence it was replaced in Paper II by the V -band light curve. The upper-middle and lower-middle panels show the results of the spectral fitting for F_{gal} and F_{AGN} , respectively. The light curve of F_{AGN} is basically identical to that of the V -band (bottom panel). Clearly, the unrealistic high F_{5100} around JD 2456300 was caused by the large contribution of the host galaxy caused by seeing and guiding fluctuations. On other JDs, the host contamination is relatively small, but still strong enough to affect the variability of F_{AGN} , e.g., the peak around JD 2456250.

B. FE II LIGHT CURVES MEASURED BY INTEGRATION

We present the Fe II light curves measured by the traditional integration method for a comparison with that by the present fitting scheme in this Appendix. The flux of the Fe II bump on the red side of [O III] $\lambda 5007$ is calculated by integrating in 5115–5465 Å the flux above the straight line set by two continuum windows 5085–5115 and 5465–5495 Å (the three bands are in the rest frame). Figure 10 shows these light curves. Comparing with those given by the fitting method (in Figures 4 and 5), all the light curves by integration show larger scatter. For four objects (Mrk 1044, Mrk 142, MCG +06–26–012, and IRAS F12397+3333), rough structures can be recognized in their light curves, and the derived Fe II time lags are consistent with those given by the fitting but with larger uncertainties. The remaining objects fail to have reliable measurement of time lag, for their scattered light curves without clear structures. We also tried to measure the flux of the Fe II bump on the blue side of $H\beta$ by choosing an integration interval avoiding the broad He II line. Similarly, light curves with poor quality are obtained.

REFERENCES

- Baldwin, J. A., Ferland, G. J., Korista, K. T., Hamann, F., & LaCluyzé, A. 2004, *ApJ*, 615, 610
- Barth, A. J., Pancoast, A., Bennert, V. N., et al. 2013, *ApJ*, 769, 128
- Barth, A. J., Pancoast, A., Thorman, S. J., et al. 2011, *ApJ*, 743, L4
- Bentz, M. C., Denney, K. D., Grier, C. J., et al. 2013, *ApJ*, 767, 149
- Bentz, M. C., Peterson, B. M., Netzer, H., Pogge, R. W., & Vestergaard, M. 2009, *ApJ*, 697, 160
- Bentz, M. C., Walsh, J. L., Barth, A. J., et al. 2010, *ApJ*, 716, 993
- Bian, W.-H., Huang, K., Hu, C., et al. 2010, *ApJ*, 718, 460
- Boksenberg, A., & Netzer, H. 1977, *ApJ*, 212, 37
- Boller, T., Brandt, W. N., & Fink, H. 1996, *A&A*, 305, 53
- Boroson, T. A. 2002, *ApJ*, 565, 78
- Boroson, T. A., & Green, R. F. 1992, *ApJS*, 80, 109
- Bruzual, G., & Charlot, S. 2003, *MNRAS*, 344, 1000
- Cardelli, J. A., Clayton, G. C., & Mathis, J. S. 1989, *ApJ*, 345, 245
- Chelouche, D., Rafter, S. E., Cotlier, G. I., Kaspi, S., & Barth, A. J. 2014, *ApJ*, 783, L34
- Chelouche, D., & Zucker, S. 2013, *ApJ*, 769, 124
- Collin-Souffrin, S., Joly, M., Dumont, S., & Heidmann, N. 1980, *A&A*, 83, 190
- Collin, S., Kawaguchi, T., Peterson, B. M., & Vestergaard, M. 2006, *A&A*, 456, 75
- Du, P., Hu, C., Lu, K.-X., et al. 2014, *ApJ*, 782, 45 (Paper I)
- Edelson, R., Turner, T. J., Pounds, K., et al. 2002, *ApJ*, 568, 610
- Ferland, G. J., Hu, C., Wang, J.-M., et al. 2009, *ApJ*, 707, L82
- Gaskell, C. M., & Sparke, L. S. 1986, *ApJ*, 305, 175
- Gaskell, C. M., & Peterson, B. M. 1987, *ApJS*, 65, 1
- Grier, C. J., Peterson, B. M., Pogge, R. W., et al. 2012, *ApJ*, 744, L4
- Ho, L. C., & Kim, M. 2009, *ApJS*, 184, 398
- Hu, C., Wang, J.-M., Ho, L. C., et al. 2008, *ApJ*, 687, 78
- Hu, C., Wang, J.-M., Ho, L. C., et al. 2012, *ApJ*, 760, 126
- Joly, M. 1987, *A&A*, 184, 33
- Kaspi, S., Maoz, D., Netzer, H., et al. 2005, *ApJ*, 629, 61
- Kaspi, S., Smith, P. S., Netzer, H., et al. 2000, *ApJ*, 533, 631
- Kollatschny, W., Bischoff, K., & Dietrich, M. 2000, *A&A*, 361, 901
- Koratkar, A. P., & Gaskell, C. M. 1991, *ApJS*, 75, 719
- Kuehn, C. A., Baldwin, J. A., Peterson, B. M., & Korista, K. T. 2008, *ApJ*, 673, 69
- Maoz, D., & Netzer, H. 1989, *MNRAS*, 236, 21
- Maoz, D., Netzer, H., Leibowitz, E., et al. 1990, *ApJ*, 351, 75
- Maoz, D., Netzer, H., Peterson, B. M., et al. 1993, *ApJ*, 404, 576
- Netzer, H. 1990, in *Active Galactic Nuclei*, ed. R. D. Blandford, H. Netzer, & L. Woltjer (Berlin: Springer), 137
- Netzer, H., & Wills, B. J. 1983, *ApJ*, 275, 445
- O'Donnell, J. E. 1994, *ApJ*, 422, 158
- Onken, C. A., Ferrarese, L., Merritt, D., et al. 2004, *ApJ*, 615, 645
- Osterbrock, D. E., & Pogge, R. W. 1985, *ApJ*, 297, 166
- Peterson, B. M., Denney, K. D., De Rosa, G., et al. 2013, *ApJ*, 779, 109
- Peterson, B. M., Ferrarese, L., Gilbert, K. M., et al. 2004, *ApJ*, 613, 682
- Peterson, B. M., Wanders, I., Horne, K., et al. 1998, *PASP*, 110, 660
- Press, W. H., Teukolsky, S. A., Vetterling, W. T., & Flannery, B. P. 1992, *Numerical Recipes in FORTRAN* (2nd ed., Cambridge: Cambridge Univ. Press)
- Rafter, S. E., Kaspi, S., Chelouche, D., et al. 2013, *ApJ*, 773, 24

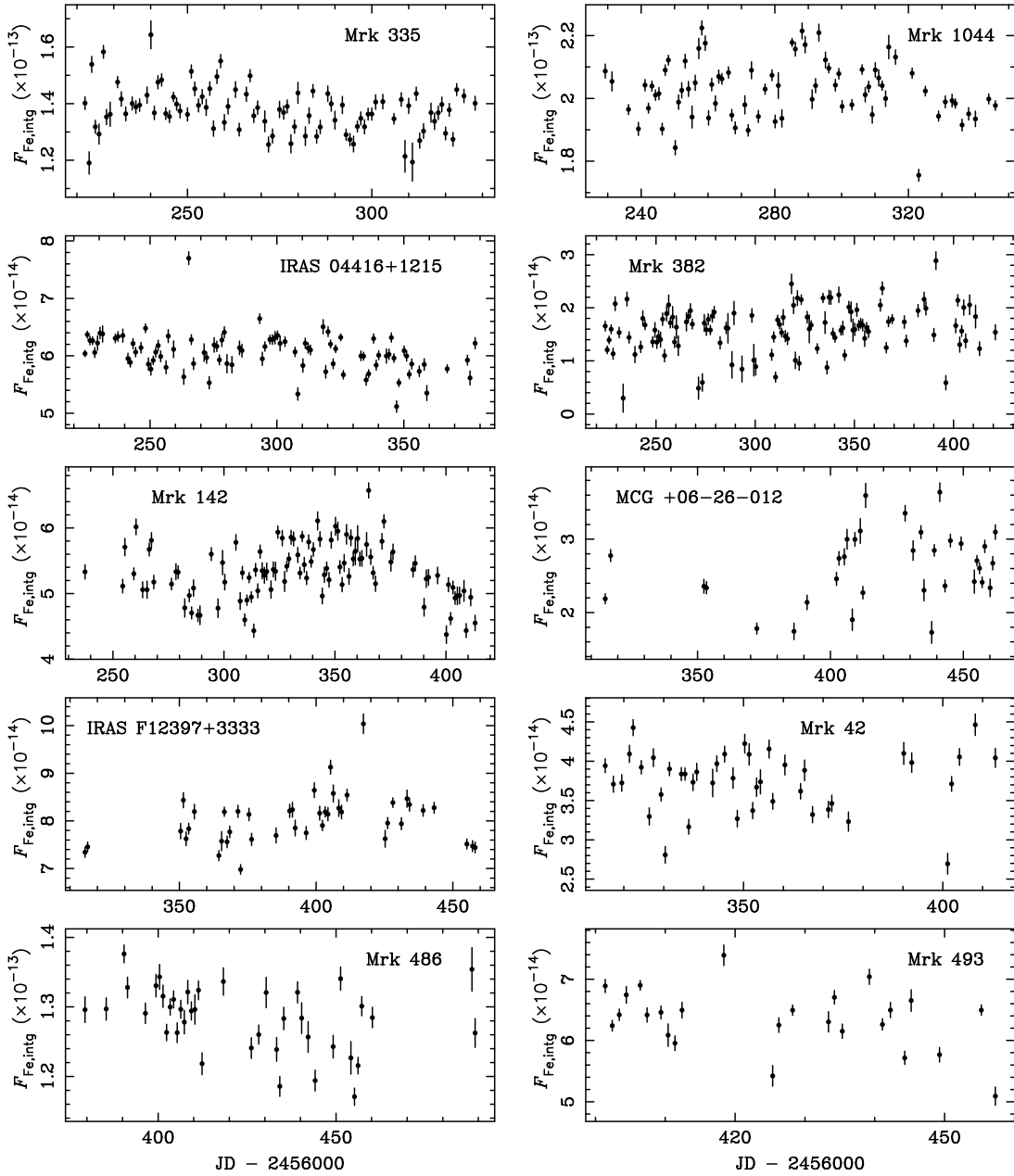


Figure 10. Light curves of Fe II measured by simple integration ($F_{\text{Fe,intg}}$). All have larger scatter comparing with those obtained by fitting shown in Figures 4 and 5.

Richards, G. T., Kruczek, N. E., Gallagher, S. C., et al. 2011, *AJ*, 141, 167
 Rodríguez-Pascual, P. M., Alloin, D., Clavel, J., et al. 1997, *ApJS*, 110, 9
 Schlafly, E. F., & Finkbeiner, D. P. 2011, *ApJ*, 737, 103
 Shapovalova, A. I., Popovic, L. C., Burenkov, A. N., et al. 2012, *ApJS*, 202, 10
 Shen, Y., & Ho, L. C. 2014, *Nature*, 513, 210
 Sigut, T. A. A., & Pradhan, A. K. 1998, *ApJ*, 499, L139
 Sulentic, J. W., Marziani, P., & Dultzin-Hacyan, D. 2000, *ARA&A*, 38, 521
 Vanden Berk, D. E., Richards, G. T., Bauer, A., et al. 2001, *AJ*, 122, 549
 Van der Marel, R. P., & Franx, M. 1993, *ApJ*, 407, 525
 Véron-Cetty, M.-P., Joly, M., & Véron, P. 2004, *A&A*, 417, 515
 Vestergaard, M., & Peterson, B. M. 2005, *ApJ*, 625, 688

Wang, J., Wei, J. Y., & He, X. T. 2005, *A&A*, 436, 417
 Wang, J.-M., Du, P., Hu, C., et al. 2014, *ApJ*, 793, 108 (Paper II)
 Wang, J.-M., Du, P., Valls-Gabaud, D., Hu, C., & Netzer, H. 2013, *Phys. Rev. Lett.*, 110, 81301
 Wang, J.-M., Watarai, K.-Y., & Mineshige, S. 2004, *ApJ*, 607, L107
 White, R. J., & Peterson, B. M. 1994, *PASP*, 106, 879
 Wills, B. J., Netzer, H., & Wills, D. 1985, *ApJ*, 288, 94
 Woo, J.-H., Schulze, A., Park, D., et al. 2013, *ApJ*, 772, 49
 York, D. G., Adelman, J., Anderson, J. E., et al. 2000, *AJ*, 120, 1579
 Zhang, X.-G. 2013, *MNRAS*, 435, 2141
 Zhou, H., Wang, T., Yuan, W., et al. 2006, *ApJS*, 166, 128